Received 18 June 2024, accepted 11 July 2024, date of publication 16 July 2024, date of current version 1 October 2024.
Digital Object Identifier 10.1109/ACCESS.2024.3429208

RESEARCH ARTICLE

Design of a Dual-Band Shared-Aperture Array Antenna Composed of Array Elements With High Electromagnetic Transparency

JIYOUNG PARK[1], DOYOUNG JANG[2], HOSUNG CHOO[1], (Senior Member, IEEE), AND SUNGSIK WANG[3], (Senior Member, IEEE)
[1]Department of Electronic and Electrical Engineering, Hongik University, Seoul 04066, South Korea
[2]Hanwha Systems Company Ltd., Yongin 17121, South Korea
[3]Department of Electrical, Electronic, and Communication Engineering, Hanyang Cyber University, Seoul 04763, South Korea

Corresponding author: Sungsik Wang (kingwss@hycu.ac.kr)

This work was supported in part by Korea Research Institute for Defense Technology Planning and Advancement (KRIT) Grant funded by Korea Government (Defense Acquisition Program Administration—DAPA) (Space Signal Intelligence Research Laboratory, in 2022) under Grant KRIT-CT-22-021; in part by the Basic Science Research Program through the National Research Foundation of Korea (NRF) funded by the Ministry of Education under Grant 2015R1A6A1A03031833; and in part by the NRF Grant funded by Korea Government (MSIT) under Grant 2022R1G1A1012774.

ABSTRACT In this paper, we propose a dual-band shared-aperture antenna composed of array elements with high electromagnetic (EM) transparency. To increase EM transparency, the antenna consists of an optimized substrate with low effective permittivity by combining thin dielectric sheets and air-gap layers. To further improve the EM transparency, thin dual-loop radiators with optimized widths and lengths are adopted for the S-band element, and an E-shaped patch antenna is employed for an X-band element. This configuration minimize the pattern distortion in the X-band elements while enhancing antenna bandwidths. In addition, a calibration layer comprising four monopole probes and microstrip transmission lines is included for monitoring the phase and amplitude errors of each element. To verify the feasibility, the proposed antenna is fabricated to measure antenna characteristics, such as reflection coefficients, beam steering performance, and mutual coupling in a full anechoic chamber. The fractional bandwidths of the antenna in the S- and X-bands are 16.4% and 26.8%, respectively. The array gains at the bore-sight are 16.0 dBi in the S-band and 24.0 dBi in the X-band.

INDEX TERMS Radar, shared-aperture, array antenna, S-band, X-band.

I. INTRODUCTION

With the rapid advancement of radar technologies, multi-function radars (MFRs) that can simultaneously detect and track multiple targets using S- and X-band radars have been extensively employed in military applications [1], [2], [3], [4], [5], [6], [7]. In conventional MFRs, S-band and X-band radars are separately mounted on the mast of a military ship, thus requiring a large mounting area. To reduce the mounting area, multi-layered shared-aperture antennas in which an S-band radar is stacked on top of an X-band radar have recently been reported [8], [9], [10], [11]. However, the top-placed S-band elements of these shared-aperture antennas have thick antenna substrates, which can generate unwanted surface wave modes and cause pattern distortion in the bottom-placed X-band elements. To solve the problem, quasi-air substrates with thick air gaps can be adopted for S-band elements [12], [13], [14]. Since these substrates can suppress unwanted surface wave modes, the electromagnetic (EM) transparency of an S-band element can be improved. Nevertheless, pattern distortion remains because of the sizable conductive surface of S-band elements. To further enhance EM transparency of the S-band element, various studies have been conducted by employing small radiators such as monopoles, dipoles, and

The associate editor coordinating the review of this manuscript and approving it for publication was Kai-Da Xu.

loops for the S-band elements [15], [16], [17], [18], [19], [20]. However, since reducing the radiator size often results in bandwidth decrease due to the high-quality factor of the radiator, it is important to design a radiator that achieves maximum bandwidth while minimizing blockage from an S-band radiator [21]. Furthermore, to monitor and precisely compensate for beam forming errors in phased array radar, a calibration probe should be also considered [22], [23].

In this paper, we propose an S/X-band shared-aperture array antenna composed of array elements with high EM transparency. The proposed array antenna consists of S-band, X-band, and calibration layers. The S-band layers, which are equipped with air-gap layers, are stacked onto the X-band layer. Since radiation patterns of X-band elements can be distorted by S-band elements, high EM transparent structures are employed for the antenna substrate and the conductive radiators of the S-band elements. The S-band antenna substrate has the thin dielectric sheets and the thick air-gap layers. A perforated 3D printed resin structure is employed to form the robust air-gap layer. Since the permittivity of the S-band substrate is reduced close to 1 by the thick air-gap layers, generation of unwanted surface waves can be effectively suppressed. To further achieve high EM transparency, loop radiators with optimized widths and lengths are applied to the S-band elements. These thin loop radiators minimize radiation blocking between the S- and X-band elements, thereby reducing pattern distortion in the X-band. In addition, the S- and X-band elements have coupled-fed dual-loop structures and E-shaped patch structures, respectively, which maintain broadband characteristics while reducing the radiator size. The combination of the loop and E-shaped antennas is the design that can achieve high EM transparency by minimizing blockage effect between radiators. This configuration is adopted for the first time in this work, unlike previous shared-aperture radars. Furthermore, to precisely compensate for beam forming errors, an additional calibration layer consisting of monopole probes and transmission lines is proposed. This calibration layer is inserted below an X-band layer to monitor abnormal input signals in real time. The calibration layer consists of four probes that collect coupling signals from each array element and microstrip lines that transmit the signals to a calibration port. The transmitted coupling signals are used to determine compensation values, which can maintain the beam forming performance of the radar system. The S-band, X-band, and calibration layers combine to create an entire antenna part, which is then connected to transmit/receive modules (TRMs) for beam steering control. To verify the feasibility of the proposed antenna, its reflection coefficients and beam steering performance in the S- and X- bands are investigated. Mutual coupling between the calibration port and each element are also measured.

II. DESIGN OF THE SHARED-APERTURE ARRAY ANTENNA

Fig. 1 illustrates the geometry of the proposed shared-aperture array antenna. As shown in Fig. 1(a), the antenna has a stacked structure, wherein dual-loop S-band elements

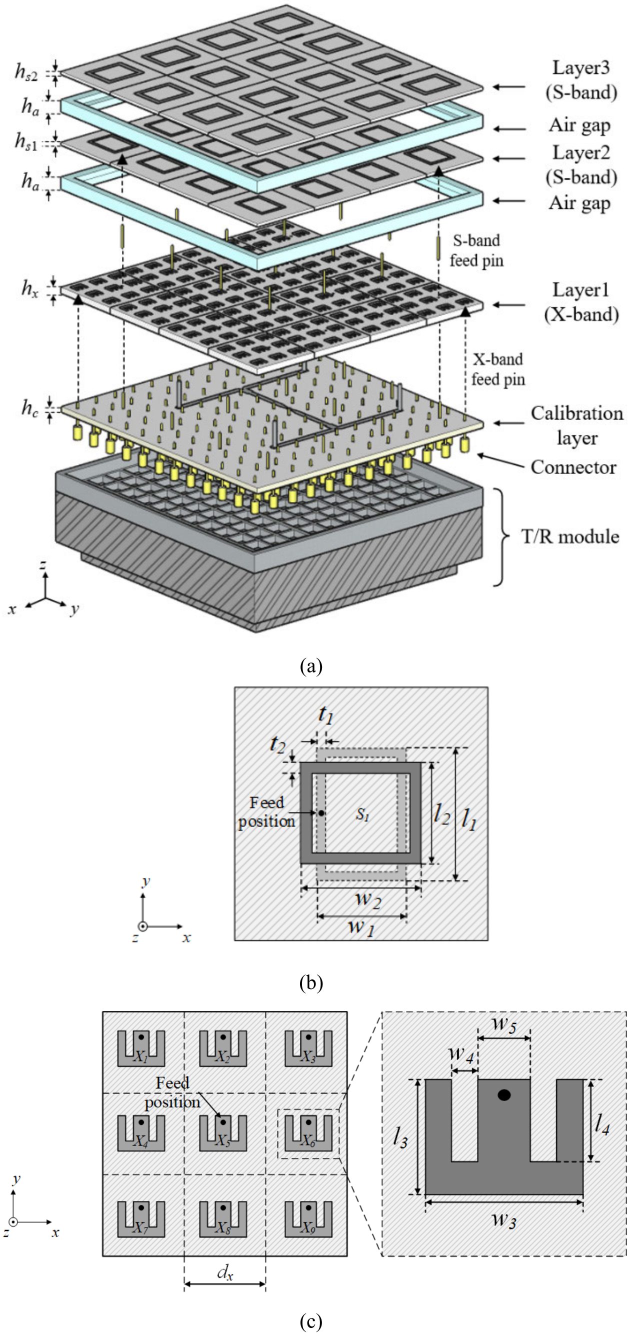

FIGURE 1. **Geometry of the proposed antenna. (a) Configuration of the multilayered shared-aperture antenna. (b) Top view of an S-band element. (c) Top view of the X-band array.**

(layers 2 and 3) are stacked onto X-band E-shaped patch elements (layer 1). To prevent the degradation of radiation characteristics in the X-band elements owing to the stacking of the S-band elements, the substrates and radiators of the S-band elements are optimized to achieve high EM transparency. The stacked structure in the S-band comprises two sets of thin RF-35 dielectric sheets ($\varepsilon_r = 3.5$, $\tan\delta = 0.0018$) and air-gap layers. To form a robust air-gap layer beneath the thin dielectric sheet, a perforated 3D-printed structure made of 2.5 mm thick resin is employed. This S-band

TABLE 1. Design parameters of the proposed antenna.

Parameters	Optimized values (mm)
l_1	29.5
l_2	24.2
l_3	6.5
l_4	6
w_1	17.2
w_2	29.5
w_3	7
w_4	0.8
w_5	2.7
t_1	1.5
t_2	2.2
d_s	51
d_x	17
h_{s1}	0.5
h_{s2}	0.5
h_a	2.5
h_x	1.6
h_c	1.6

substrate can improve EM transparent characteristics because of its reduced effective permittivity and can also broaden the bandwidth in the S-band by increasing the volume of the element. The antenna is also modularized with a unit cell that consists of one S-band element and 3 × 3 X-band elements. This proposed unit cell combining the loop and the E-shaped antennas is the design that can achieve high transparency by minimizing blockage effect between radiators. The 4 × 4 unit cells are then expanded to the entire array, which is advantageous for maintenance. Fig. 1(b) shows the top view of the S-band layer in one unit cell. The S-band element is a thin dual-loop antenna whose length, width, and thickness are l_1, l_2; w_1, w_2; and t_1, t_2, respectively. The loop radiator for the proposed S-band element has a structure similar to an annular ring or a rectangular patch with a rectangular slot at the center to minimize the blockage effect. This antenna employs a rectangular slot to lengthen surface current paths, and thus reducing the size of the element [24]. The S-band loop element is designed for the fundamental TM_{11} mode assuming the S-band loop as an annular ring. Typically, the average circumference of an annular ring antenna matches the guiding wavelength of the microstrip used [25]. The proposed antenna is designed with dual loop radiators having circumferences of 0.99λ and 0.95λ, based on a center frequency of 3.05 GHz. Since the thin loop radiator minimizes the radiation blocking between S and X-band elements, EM transparency can be maximized. Furthermore, the coupled-fed dual-loop antenna improves bandwidth while maintaining a thin loop geometry. Fig. 1(c) presents the top view of a unit cell for the X-band layer. The E-shaped patch is employed for the X-band element that has a length l_3 and a width w_3. The length and width of the slot are l_4 and w_4, respectively, and the spacing between slots is w_5. Because an E-shaped patch has various current paths due to its slots, it has broadband characteristics while maintaining a low profile in the X-band layer. At the bottom of the X-band layer is a calibration layer intended to monitor the status of each element in real time, with which abnormal phase and amplitude errors can be appropriately compensated. The calibration port monitors the status of each element through coupling, and thus the calibration layer consists of four monopole probes and microstrip transmission lines. The entire antenna part is completed by assembling the S-band, X-band, and calibration layers with a metal frame. Finally, the antenna part is attached to the TRMs for beam steering control. Each element is fed with different phases and amplitudes by TRMs, allowing for precise control of the beam's direction and shape. The optimized design parameters are listed in Table 1.

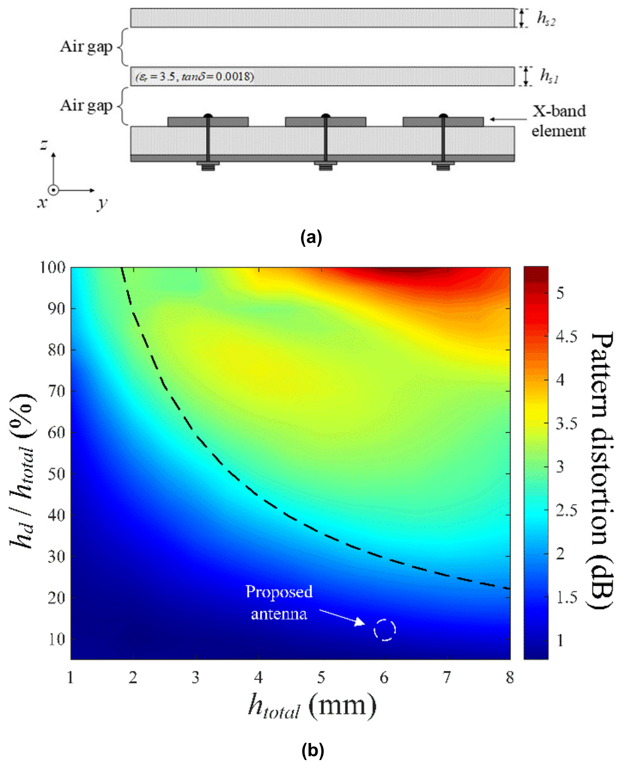

FIGURE 2. The pattern distortion in the X-band element according to the S-band substrate. (a) Geometry of dielectric sheets in the S-band elements stacked onto the X-band array. (b) Average pattern distortion.

Fig. 2 illustrates the pattern distortion in the X-band elements according to the structure of the S-band substrate. The S-band substrate is stacked onto the X-band array as shown in Fig. 2(a). The S-band substrate is composed of RF-35 dielectric sheets and air-gap layers. The heights of the dielectric sheets for the S-band are h_{s1} and h_{s2}. Dielectric substrate height h_d is calculated using $h_{s1} + h_{s2}$, and total substrate height h_{total} is the sum of h_d and an air-gap. In the stacked structure, the electromagnetic waves radiated by an

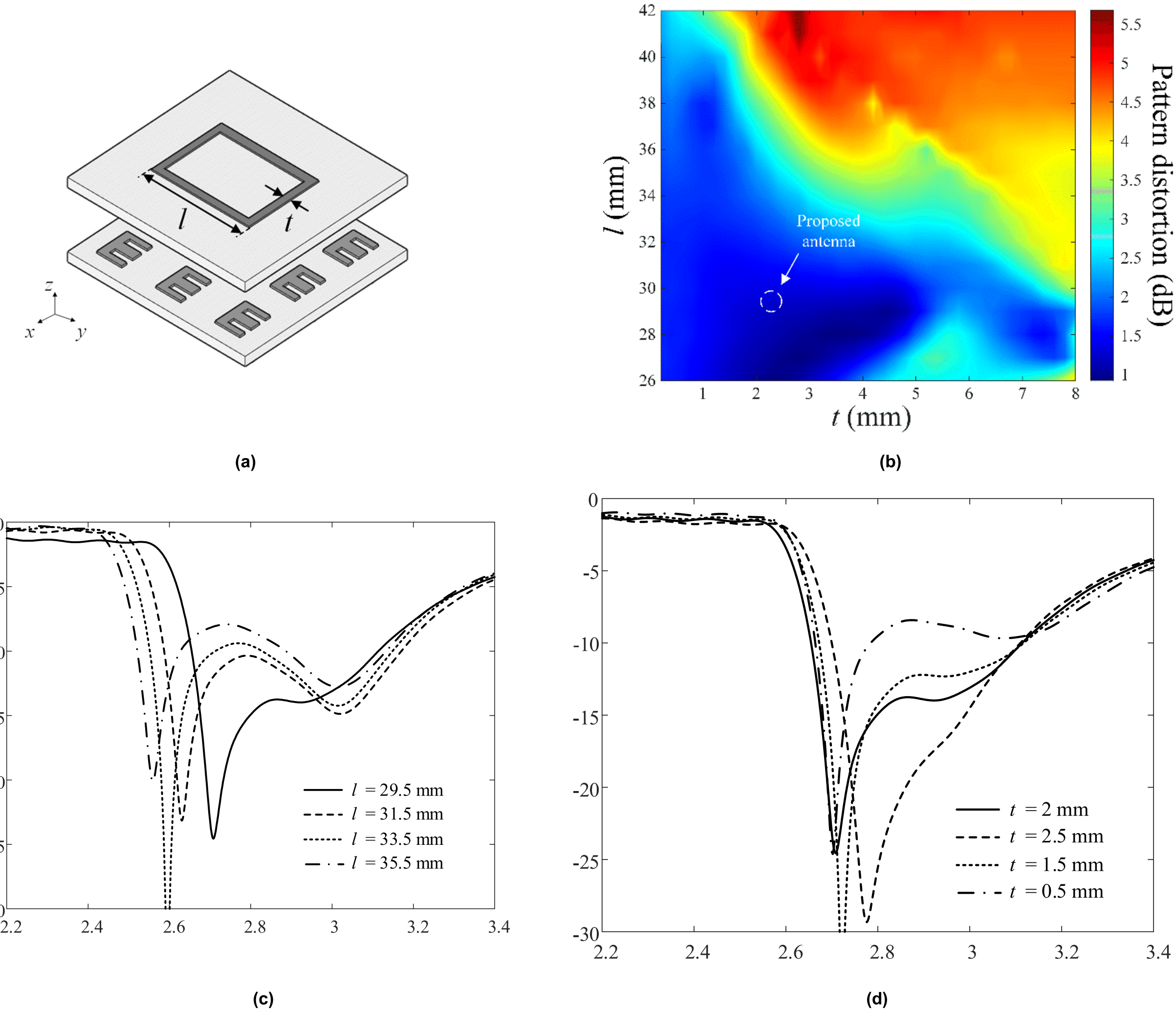

FIGURE 3. **EM transparency and bandwidth according to the S-band loop size. (a) Geometry. (b) Average pattern distortion in the X-band element (c) Comparisons of reflection coefficients depending on the length *l*. (d) Comparisons of reflection coefficients depending on the thickness *t*.**

X-band element pass through the overlying S-band substrate so that unwanted surface waves can be generated due to the thickness of the dielectric substrate. The dielectric substrate thickness at which the dominant TE surface mode occurs is derived by the following equation [26]:

$$TE_1 : h_t = \frac{c}{4f_c\sqrt{\varepsilon_e - 1}} \tag{1}$$

where f_c is the cutoff frequency, $\boldsymbol{\varepsilon_e}$ denotes the effective relative permittivity of the substrate, and c is the speed of light in free space. When the thickness of the substrate exceeds h_t, the pattern of the X-band radiator is severely distorted because of the induced surface waves. Fig. 2(b) depicts pattern distortion in the central element of the X-band according to h_{total} and h_d/h_{total}. The pattern distortion in the X band is determined thus [27]:

$$\text{Pattern distortion (dB)} = 10\log_{10}\frac{\int_0^{2\pi}\int_0^{\frac{\pi}{2}}|F_o(\theta,\phi) - F_c(\theta,\phi)|\,d\theta d\phi}{2\pi} \tag{2}$$

where F_0 refers to the radiation pattern of the X-band element without S-band dielectric sheets ($h_d = 0$), and F_c refers to the radiation pattern of the X-band element with S-band dielectric sheets. Pattern distortion is defined as the average difference in radiation patterns in the hemispheric region in the +z direction. As expected, significant pattern distortion occurs over the dotted line h_t derived from equation (1). Below the dotted line, relatively little pattern distortion is observed, and the circle indicates the substrate height for the proposed antenna. At this point, pattern distortion is suppressed to less than 0.6 dB. Based on this parametric study, an optimized S-band substrate consists of two RF-35 dielectric sheets (h_{s1}, h_{s2} = 0.5 mm) and two air-gap layers (h_a = 2.5 mm).

Fig. 3 depicts the analysis for the EM transparency and bandwidth according to the S-band loop size. Fig. 3(a) illustrates the geometry of the S-band loop radiator located on top of the X-band elements, where l and t are the length and thickness of the S-band loop radiator, respectively. As shown

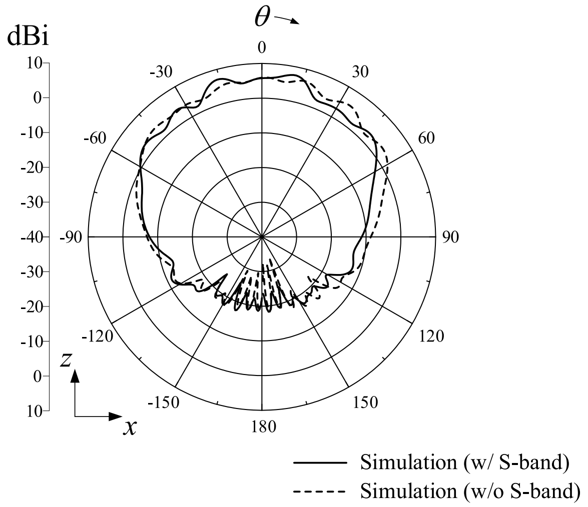

FIGURE 4. Active element pattern of a central X-band element.

in Fig. 3(b), pattern distortion in the central element of the X-band varies according to l and t. As t and l increases, the area of the S-band loop that blocks radiation in the X-band elements expands, which naturally elevates the pattern distortion. Fig. 3(c) shows reflection coefficients depending on the S-band loop length l within the range where the S-band loop radiator does not obscure the X-band element. The bandwidth characteristics are investigated by varying l from 29.5 mm to 35.5 mm in 2 mm increments, while keeping the loop circumference constant. As the l increases, the matching characteristics deteriorate at the center of the target band (3.05 GHz). Fig. 3(d) provides reflection coefficients according to the loop thickness t (from 2.5 mm to 0.5 mm). When the t decreases, the matching characteristics also deteriorate. The shape of the S-band loop radiator is then optimized for $l = 29.5$ mm and $t = 2.2$ mm, which generated a pattern distortion of less than 1.2 dB.

Fig. 4 presents a comparison between the active element patterns (central X-band element) with and without the S-band element. The bore-sight gains with and without the S-band structure are 5.7 dBi and 5.9 dBi, respectively. The pattern distortion occurs 1.2 dB in the comparison. This demonstrates that the proposed S-band antenna element maintains electromagnetic transparency and does not significantly affect the performance of the X-band antenna.

III. VERIFICATION OF THE PROPOSED ANTENNA

To verify the feasibility of the proposed antenna, the array antenna is fabricated and measured in a full anechoic chamber. The array spacings in the S- and X-band elements are 51 mm (0.52λ at 3.05 GHz) and 17 mm (0.54λ at 9.5 GHz), respectively. Fig. 5 displays the fabricated array antenna parts, which are S-band layers, an X-band layer, a calibration layer, and a metal frame. A front view of the antenna is provided in Fig. 5(a), showing the top S-band layer, which contains 4 × 4 S-band array elements. Fig. 5(b) shows the second S-band layer, where the S-band feed pin is connected to the loop radiator. The perforated 3D printed resin frame is fabricated to form the robust air-gap layer beneath the S-band dielectric sheet, as shown in Fig. 5(c). Fig. 5(d) shows the X-band layer, which consists of 12 × 12 X-band array elements. Holes in the X-band layer allow the S-band feed

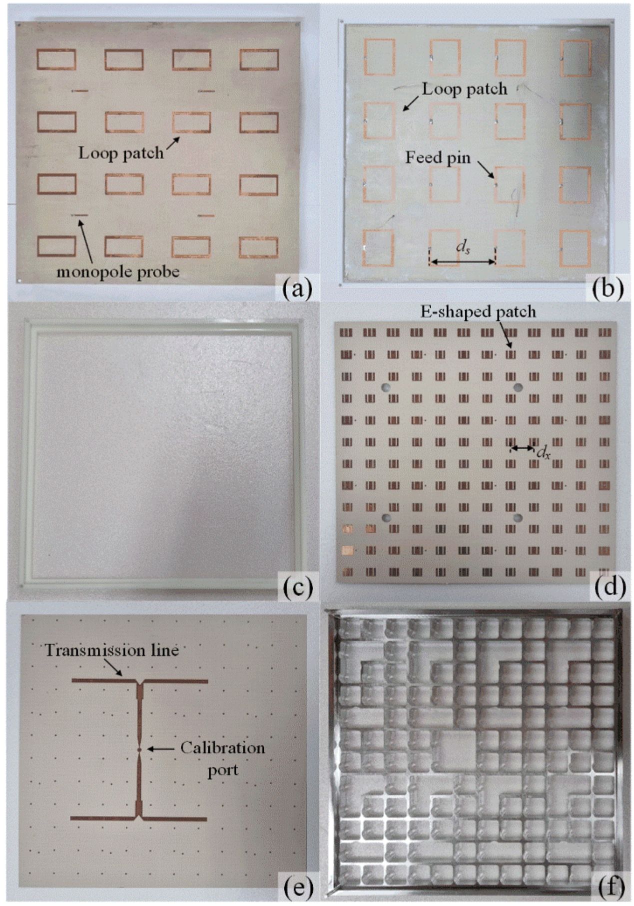

FIGURE 5. Photograph of the fabricated array antenna. (a) Top view of the proposed antenna (S-band layer). (b) Top view of an S-band layer. (c) 3D printing frame for the air-gap layers. (d) Top view of the X-band layer. (e) Top view of the calibration layer. (f) Metal frame of the antenna.

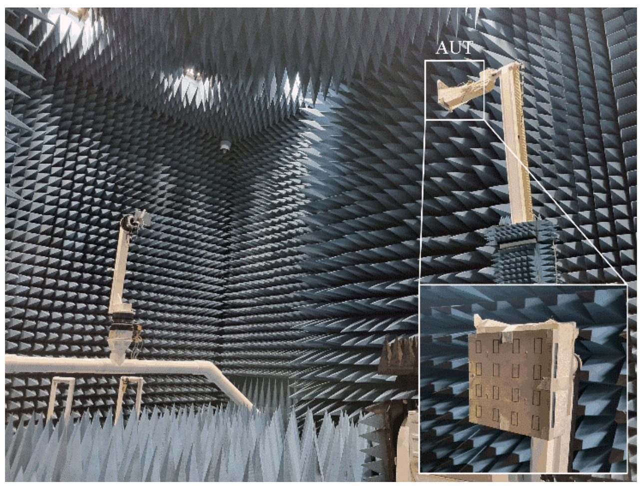

FIGURE 6. Measurement setup in the full anechoic chamber.

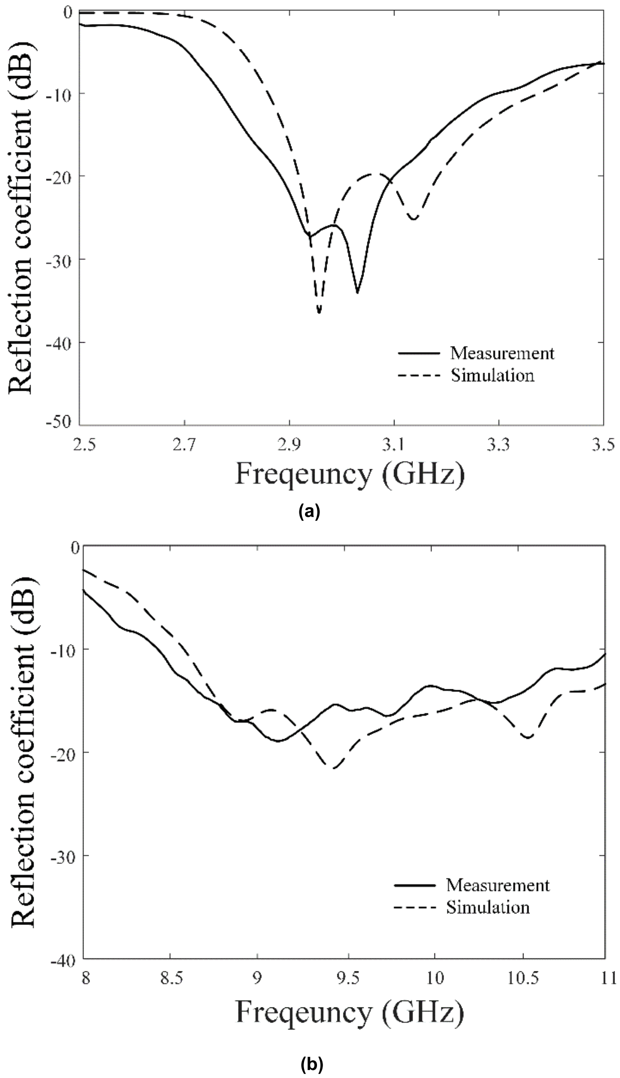

FIGURE 7. Reflection coefficients: (a) S-band element. (b) X-band element.

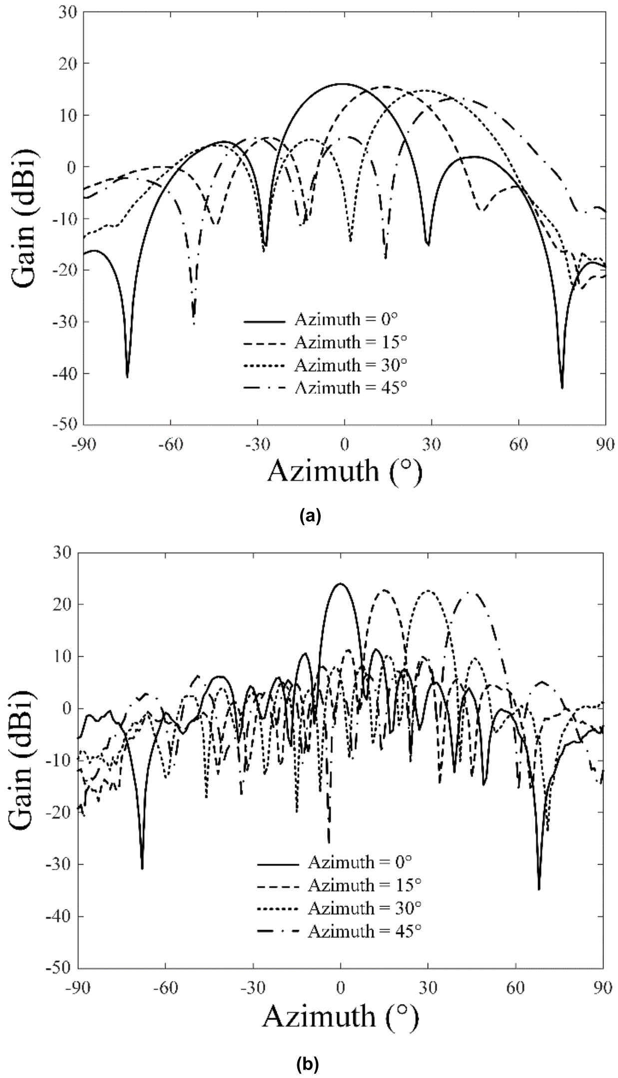

FIGURE 8. Beam steering performance of the proposed antenna (a) S-band. (b) X-band.

pins and the monopole probes to pass through. The monopole probe for calibration is connected to the calibration line on the calibration layer as shown in Fig. 5(e), with which the proposed array antenna can be monitored. All elements of the antenna are fabricated through an etching process and laminated using an adhesive film in each layer. Additionally, the metal frame connected to the bottom of the antenna firmly fixes all the layers, improving the durability of the antenna as shown in Fig. 5(f).

Fig. 6 presents the measurement setup in the full anechoic chamber. The fabricated antenna under test (AUT) is fixed with a Styrofoam jig, and the reflection coefficients and array gains of the AUT are measured to verify antenna feasibility.

Fig. 7 shows the reflection coefficients of the central elements of the S- and X-bands in the array. The solid and dashed lines indicate the measured and simulated results, respectively. The slight variation between simulation and measurement results is due to manufacturing and assembly tolerances, such as adhesive thickness and soldering during the antenna fabrication process. As indicated in Fig. 7(a), the bandwidth ($|\Gamma| < -10$ dB) of the S-band element is 16.4% (2.8 $\sim$ 3.3 GHz) which agrees well with the simulated result of 16.5%. Fig. 7(b) shows that the bandwidth of the X-band element is 26.8% (8.4 $\sim$ 11 GHz), which is also in good agreement with the simulation of 24.7%.

Fig. 8 depicts the beam steering performance of the proposed antenna at the central frequency of each band. To examine the array gain of the antenna, the active element patterns (AEPs) of the proposed array elements are measured in the full anechoic chamber [28], [29]. The total array gain is then calculated on the basis of the AEPs of all the elements using equation (3):

$$G_{array}\left(AZ, EL\right) = \frac{\sum_{n=1}^{I} \bar{w}_n \bar{g}_n \left(AZ, EL\right)}{\sqrt{\sum_{n=1}^{N} |w_n|^2}} \tag{3}$$

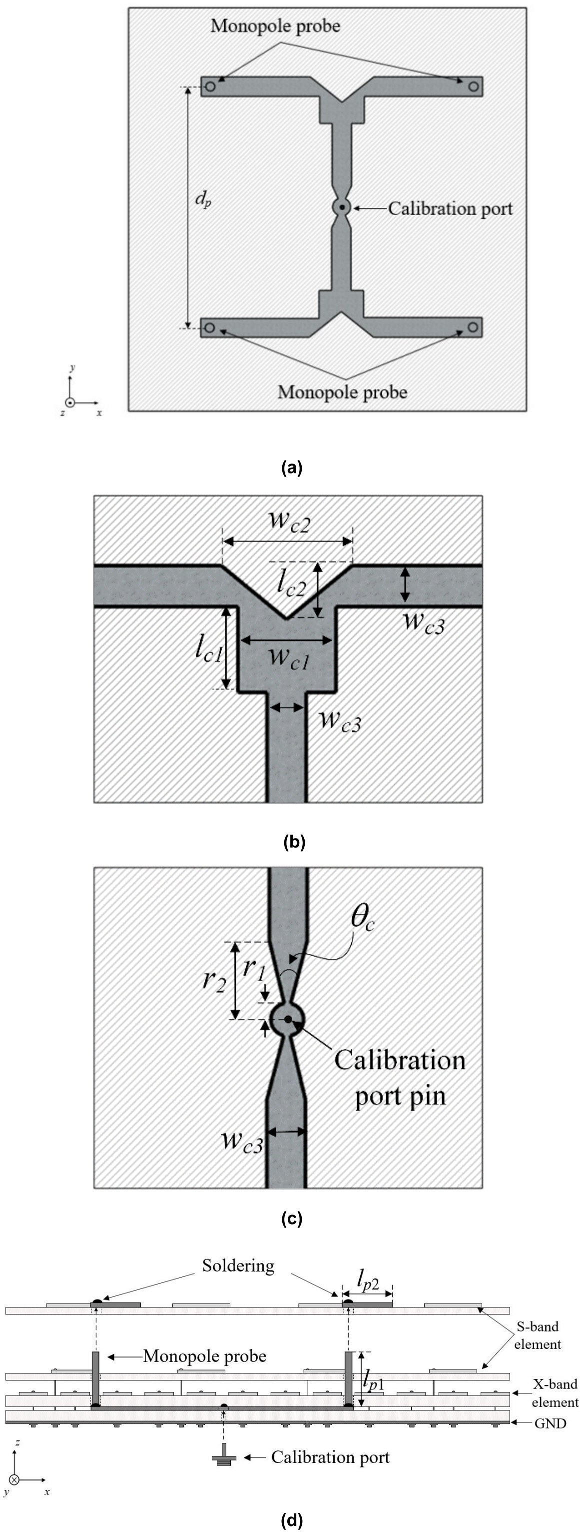

FIGURE 9. Geometry of the calibration layer. (a) Top view of the calibration layer of the proposed antenna. (b) Top view of the power divider part. (c) The calibration port pin. (d) Sideview of the antenna including the calibration layer.

where g_n is a complex AEP vector of the nth element port, and w_n is a complex weighting vector of the n^{th} element port. In the S-band, the measured array gain in the bore-sight direction is 16.0 dBi, which agrees with the simulation result of 16.7 dBi. The maximum gain varies from 16.0 dBi to 12.5 dBi when the main beam is steered from AZ = 0° to 45°. For the X-band, the measured and simulated array gains in the bore-sight direction are 24.0 dBi and 24.8 dBi, respectively. The bore-sight gains decrease from 24 dBi to 21.5 dBi under the same beam-steering conditions.

TABLE 2. Design parameters of the calibration layer.

Parameters	Values
d_p	102 mm
w_{c1}	5 mm
w_{c2}	7 mm
w_{c3}	3 mm
l_{c1}	12 mm
l_{c2}	4.5 mm
r_1	1.5 mm
r_2	10 mm
θ_c	17°
l_{p1}	7.6 mm
l_{p2}	12.6 mm

The ideal array gain with the number of elements can be calculated as following equation [30]:

$$G_{array} = G_{element} + 10\log_{10}(N) \qquad (4)$$

where N is the number of elements. Measured bore-sight gains of the central array element of the proposed antenna are 4.5 dBi in the S-band and 4.4 dBi in the X-band, respectively. Thus, when each single element is arranged in an S-band 4 × 4 array and an X-band 16 × 16 array, the ideal array gain is calculated to be 16.5 dBi for the S-band and 25.9 dBi for the X-band, which are close to the simulated and measured array gain.

Fig. 9 presents the geometry of the calibration layer located below the X-band layer. The four monopole probes and microstrip transmission lines in the calibration layer are shown in Fig. 9(a). The transmission lines are divided into four branches from the calibration port, and each monopole probe is located at each end of the line. The four monopole probes collect coupling signals from each array element, and their spacing d_c is adjusted for appropriate coupling strengths between the probe and each array element. The calibration port then monitors the status of each element by monitoring the coupling. The detailed geometry of the power divider, where two lines are divided into four lines, is shown in Fig. 9(b). The design parameters are listed in Table 2. The transition for power distribution is determined by w_{c1} and l_{c1}. The line is split into two by w_{c3}, w_{c2}, and l_{c2}. In Fig. 9(c), the calibration port pin is connected to the center circle of the transmission line with a radius of r_1. A fan-shaped transmission with radius r_2 and angle θ_c is employed

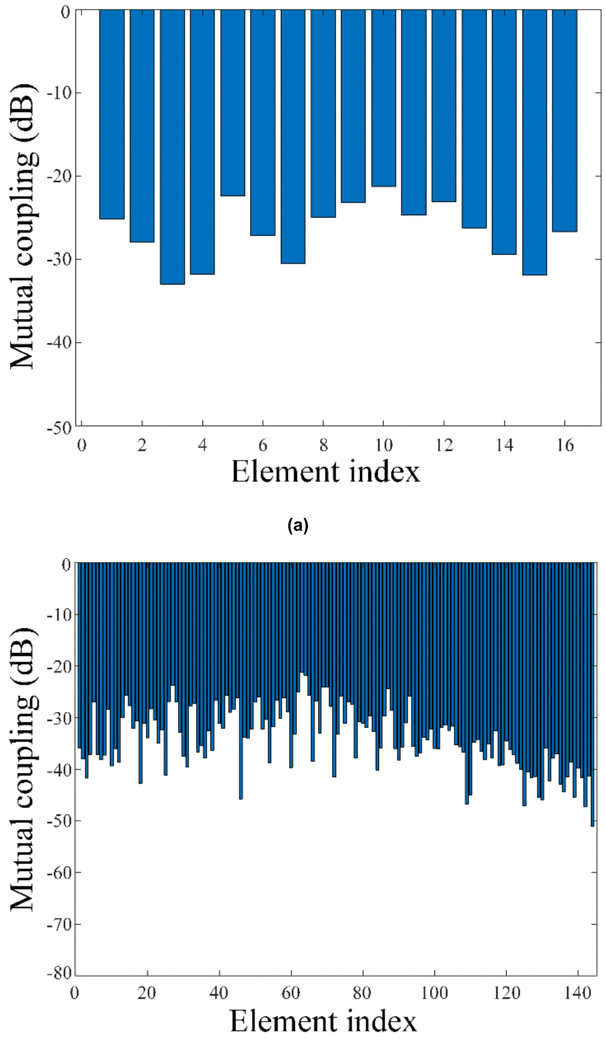

(a)

(b)

FIGURE 10. Mutual coupling between the elements and calibration port: (a) S-band and (b) X-band.

for impedance matching between the central circle and the transmission lines. The entire array antenna, including the calibration layer, is shown in Fig. 9(d). The length ($l_{p1} + l_{p2}$) of the monopole probes is optimized to capture the coupling strength of −20 dB to −50 dB between the probe and each array element.

Fig. 10 indicates the measured coupling characteristics between the calibration port and each array element (S-band 4 × 4, X-band 16 × 16) at the center frequency of each band. The calibration port should have relatively uniform coupling values with each antenna element to ensure better calibration accuracy. The coupling levels for all the S-band elements are distributed in the range from −21.2 dB to −33.0 dB at 3.05 GHz, as shown in Fig. 10(a). At 9.5 GHz, all the X-band elements have coupling from −21.1 dB to −51.04 dB as shown in Fig. 10(b). These coupling values indicate that the calibration layer can monitor abnormal input signals in each element.

TABLE 3. Comparisons of antenna characteristics.

Research	Bandwidth	Number of elements	Height	Array gain	Scan range
[9]	S: 7.7% X: 4.8%	S: 1 X: 16	8 mm	S: 8 dBi X: 20 dbBi	< ±15°
[15]	L: 21.7% S: 11.6% X: 18.9%	L: 1 S: 4 X: 36	45 mm	L: 5 dBi S: 14 dBi X: 21dBi	-
[17]	L: < 5% S: < 5%	L: 9 S: 36	39 mm	L: 7 dBi S: 17 dBi	-
[19]	S: 1.03% X: 1.0%	S: 2 X: 28	1.8 mm	S: 9.5 dBi X: 18.3 dBi	-
[20]	S: 26.5% X: 25.2%	S: 1 X: 4	11.6 mm	S: 9 dBi X: 19.4 dBi	< ±20°
This work	S: 16.4% X: 26.8%	S: 16 X:144	9.2 mm	S: 16.0 dBi X: 24.0 dBi	< ±45°

Antenna performances are compared with other studies in Table 3. The proposed array has a low antenna profile while having more than 16% bandwidth in each band. In addition, it has an additional calibration layer, making it easier to maintain precise beamforming performance. The array gain is investigated by steering the beam up to ±45° in the azimuthal direction.

IV. CONCLUSION

We investigated a dual-band shared-aperture array antenna composed of array elements with high EM transparency. The unit cell of the proposed antenna consists of one S-band dual-loop element and an array of 3 × 3 X-band E-shaped elements. The 4 × 4 unit cells were expanded to form the entire array. The S-band elements were designed with a substrate layer that combines air-gap layers with thin dielectric sheets. These elements also had thin loop radiators with optimized widths and lengths. The fractional bandwidths of the antenna were 16.4% and 26.8% in the S- and X-bands, respectively. The maximum array gains of the S-band elements varied from 16.0 dBi to 12.5 dBi when the main beam was steered from 0° to 45°. Under the same conditions, the maximum gain in the X-band decreased from 24 dBi to 21.5 dBi. Mutual coupling between the calibration port and each element ranged from −21.2 dB to −33.0 dB at 3.05 GHz and from −21.1dB to −51.04 dB at 9.5 GHz. The results demonstrated that the proposed shared-aperture antenna was suitable for MFR applications.

REFERENCES

[1] P. W. Moo and D. J. DiFilippo, "Multifunction RF systems for naval platforms," *Sensors*, vol. 18, no. 7, p. 2076, Jun. 2018.

[2] Z. Qamar, J. L. Salazar-Cerreno, and N. Aboserwal, "An ultra-wide band radome for high-performance and dual-polarized radar and communication systems," *IEEE Access*, vol. 8, pp. 199369–199381, 2020.

[3] J. E. Stailey and K. D. Hondl, "Multifunction phased array radar for aircraft and weather surveillance," *Proc. IEEE*, vol. 104, no. 3, pp. 649–659, Mar. 2016.

[4] Y. Al-Alem, L. Albasha, and H. Mir, "High-resolution on-chip *S*-band radar system using stretch processing," *IEEE Sensors J.*, vol. 16, no. 12, pp. 4749–4759, Jun. 2016.

[5] X. Chen and W. Huang, "Spatial–temporal convolutional gated recurrent unit network for significant wave height estimation from shipborne marine radar data," *IEEE Trans. Geosci. Remote Sens.*, vol. 60, 2022.

[6] Y. Wang and W. Huang, "An algorithm for wind direction retrieval from X-band marine radar images," *IEEE Geosci. Remote Sens. Lett.*, vol. 13, no. 2, pp. 252–256, Feb. 2016.

[7] M.-J. Kim, S. Lim, and D.-C. Shin, "Analysis method for determining optimal synthetic aperture time using estimated range and Doppler cone angle at the center of synthetic aperture length," *J. Electromagn. Eng. Sci.*, vol. 23, no. 3, pp. 205–211, May 2023.

[8] C. X. Bai, Y. J. Cheng, Y. R. Ding, and J. F. Zhang, "A metamaterial-based S/X-band shared-aperture phased-array antenna with wide beam scanning coverage," *IEEE Trans. Antennas Propag.*, vol. 68, no. 6, pp. 4283–4292, Jun. 2020.

[9] V. K. Kothapudi and V. Kumar, "A multi-layer S/X-band shared aperture antenna array for airborne synthetic aperture radar applications," *Int. J. RF Microw. Comput-Aid. Eng.*, vol. 31, no. 8, pp. 1–14, Aug. 2021.

[10] K. Wang, X. Liang, W. Zhu, J. Geng, J. Li, Z. Ding, and R. Jin, "A dual-wideband dual-polarized aperture-shared patch antenna with high isolation," *IEEE Antennas Wireless Propag. Lett.*, vol. 17, pp. 735–738, 2018.

[11] J. Kim, S. K. Hong, and B. Kim, "A shared-aperture S/X dual broadband microstrip antenna with one perforated patch," *Microw. Opt. Technol. Lett.*, vol. 62, no. 1, pp. 507–513, Jan. 2020.

[12] D. Jang, J.-Y. Lee, and H. Choo, "Design of a stacked dual-patch antenna with 3D printed thick quasi-air substrates and a cavity wall for wideband applications," *Appl. Sci.*, vol. 14, no. 4, p. 1571, Feb. 2024.

[13] Y. She, J. Hirokawa, M. Ando, D. Hanatani, and M. Fujimoto, "LTCC oversized rectangular waveguide slot array antenna with air layers," *IEEE Trans. Antennas Propag.*, vol. 63, no. 12, pp. 5850–5854, Dec. 2015.

[14] L. Chang, Z. Zhang, Y. Li, and M. F. Iskander, "Air substrate slot array based on channelized coplanar waveguide," *IEEE Antennas Wireless Propag. Lett.*, vol. 16, pp. 892–895, 2017.

[15] K. Li, T. Dong, and Z. Xia, "A broadband shared-aperture L/S/X-band dual-polarized antenna for SAR applications," *IEEE Access*, vol. 7, pp. 51417–51425, 2019.

[16] X. Qu, S. Zhong, Y. Zhang, and W. Wang, "Design of an S/X dual-band dual-polarised microstrip antenna array for SAR applications," *IET Microw., Antennas Propag.*, vol. 1, no. 2, pp. 513–517, Apr. 2007.

[17] K. Naishadham, R. Li, L. Yang, T. Wu, W. Hunsicker, and M. Tentzeris, "A shared-aperture dual-band planar array with self-similar printed folded dipoles," *IEEE Trans. Antennas Propag.*, vol. 61, no. 2, pp. 606–613, Feb. 2013.

[18] G. Kwon, J. Park, D. Kim, and K. C. Hwang, "Optimization of a shared-aperture dual-band transmitting/receiving array antenna for radar applications," *IEEE Trans. Antennas Propag.*, vol. 65, no. 12, pp. 7038–7051, Dec. 2017.

[19] S.-H. Hsu, Y.-J. Ren, and K. Chang, "A dual-polarized planar-array antenna for S-band and X-band airborne applications," *IEEE Antennas Propag. Mag.*, vol. 51, no. 4, pp. 70–78, Aug. 2009.

[20] S. Wang, D. Jang, Y. Kim, and H. Choo, "Design of S/X-band dual-loop shared-aperture 2×2 array antenna," *J. Electromagn. Eng. Sci.*, vol. 22, no. 3, pp. 319–325, May 2022.

[21] D. R. Jackson and N. G. Alexopoulos, "Simple approximate formulas for input resistance, bandwidth, and efficiency of a resonant rectangular patch," *IEEE Trans. Antennas Propag.*, vol. 39, no. 3, pp. 407–410, Mar. 1991.

[22] I. Seker, "Calibration methods for phased array radars," *Proc. SPIE*, vol. 8714, pp. 1–15, May 2013.

[23] F. Zhang, H. Gao, Z. Wang, and W. Fan, "An improved complex signal-based calibration method for beam-steering phased array," *IEEE Antennas Wireless Propag. Lett.*, vol. 20, pp. 2161–2165, 2021.

[24] W. Chew, "A broad-band annular-ring microstrip antenna," *IEEE Trans. Antennas Propag.*, vol. AP-30, no. 5, pp. 918–922, Sep. 1982.

[25] R. Garg, P. Bhartia, I. J. Bahl, and A. Ittipiboon, *Microstrip Antenna Design Handbook*, Norwood, MA, USA: Artech House, 2001.

[26] D. M. Pozar, *Microwave Engineering*. Hoboken, NJ, USA: Wiley, 2011.

[27] D. Jang, S. Wang, H. Kim, and H. Choo, "Design of a shared-aperture dual-loop antenna using a mutual complementary shape to improve an electromagnetic transparent characteristics between S/X-band elements," *IEEE Access*, vol. 12, pp. 21199–21206, 2024.

[28] D. F. Kelley and W. L. Stutzman, "Array antenna pattern modeling methods that include mutual coupling effects," *IEEE Trans. Antennas Propag.*, vol. 41, no. 12, pp. 1625–1632, Dec. 1993.

[29] S. Zhang, S. Gong, Q. Gong, Y. Guan, and B. Lu, "Application of the active element pattern method for calculation of the scattering pattern of large finite arrays," *IEEE Antennas Wireless Propag. Lett.*, vol. 10, pp. 83–86, 2011.

[30] T. C. Yang, "Modal beamforming array gain," *J. Acoust. Soc. Amer.*, vol. 84, no. S1, pp. S18–S19, Nov. 1988.

JIYOUNG PARK received the B.S. degree in electronic and electrical engineering from Hongik University, Seoul, South Korea, in 2023, where she is currently pursuing the M.S. degree in electronic and electrical engineering. Her research interests include array antennas, radars, microwave systems, and satellite communications.

DOYOUNG JANG received the B.S. degree in information and telecommunication engineering from Dongyang Mirae University, Seoul, Republic of Korea, in 2018, and the M.S. and Ph.D. degrees in electronic and electrical engineering from Hongik University, Seoul, in 2020 and 2023, respectively. He was a Research Engineer with MOASOFT, Seoul, from 2015 to 2018. From 2023 to 2024, he was a Research Professor with the Metamaterial Electronic Component Research Center, Hongik University. He is currently a Senior Engineer with Hanwha Systems Company Ltd. His research interests include array antennas, radars, and electromagnetic wave propagation.

HOSUNG CHOO (Senior Member, IEEE) received the B.S. degree in radio science and engineering from Hanyang University, Seoul, South Korea, in 1998, and the M.S. and Ph.D. degrees in electrical and computer engineering from The University of Texas at Austin, in 2000 and 2003, respectively. In September 2003, he joined the School of Electronic and Electrical Engineering, Hongik University, Seoul, where he is currently a Professor. His research interests include electrically small antennas for wireless communications, reader and tag antennas for RFID, on-glass and conformal antennas for vehicles and aircraft, and array antennas for GPS applications.

SUNGSIK WANG (Senior Member, IEEE) received the B.S. and M.S. degrees in radio science and engineering from Hanyang University, Seoul, South Korea, in 1997 and 1999, respectively, and the Ph.D. degree from the Department of Electronic and Electrical Engineering, Hongik University, Seoul, in 2021. In September 2021, he joined the Department of Electrical, Electronic, and Communication Engineering, Hanyang Cyber University, Seoul, where he is currently an Assistant Professor. His research interests include the beam propagation under the abnormal atmospheric phenomenon, broadband antenna design, use of the optimization algorithm in developing antennas, and antenna arrays beamforming.